

DOI: 10.1002/chem.201204112

Strong Morphological Effect of Mn₃O₄ Nanocrystallites on the Catalytic Activity of Mn₃O₄ and Au/Mn₃O₄ in Benzene Combustion

Zhao-Yang Fei,^[a] Bo Sun,^[a] Liang Zhao,^[a] Wei-Jie Ji,^{*[a]} and Chak-Tong Au^{*[b]}

Abstract: Gold nanoparticles (3–4 nm) were deposited on Mn₃O₄ nanocrystallites with three distinct morphologies (cubic, hexagonal, and octahedral). The resulting structures were characterized, and their activities for benzene combustion were evaluated. The dominant exposed facets for the three kinds of Mn₃O₄ polyhedrons show the activity order: (103) \approx (200) > (101). A similar

activity order was derived for the interfaces between the Au and the Mn₃O₄ facet: Au/(200) \approx Au/(103) > Au/(101). The metal-support interactions be-

Keywords: benzene combustion • crystal facet • gold • manganese tetraoxide • morphology • nanostructures

tween the Au nanoclusters and specific facets of the Mn₃O₄ polyhedrons lead to a unique interfacial synergism in which the electronic modification of the Au nanoparticles and the morphology of the Mn₃O₄ substrate have a joint effect that is responsible for a significant enhancement in the catalytic activity of the Au/Mn₃O₄ system.

Introduction

The functionality of materials depends strongly on their composition, phase structure, and morphology. Materials with the same composition but different structures or morphologies can have substantially different properties.^[1–4] There have been studies on the effect of morphology on the performance of nanomaterials.^[5–7] By controlling the morphology of crystallites formed during the fabrication of transition metal oxides, active sites could be preferentially exposed.^[7,8] Supported Au nanoparticles (NPs) have attracted significant attention due to their unique catalytic properties for numerous reactions, including the combustion of volatile organic compounds (VOCs).^[9–14] The catalytic activity of Au catalysts depends critically on the size of the Au particles.^[15–20] The characteristics of the Au catalysts could be affected by the nature and morphology of the support materials^[5,21,22] as well as by the method of preparation.^[23–25] Thus, it is of great interest to study the effects of the morphology of support materials on the structural and catalytic properties of supported Au catalysts.

Manganese tetraoxide (Mn₃O₄) is an important component in catalytic systems for the oxidation of carbon monox-

ide, methane, and hydrocarbons, because of its high activity, durability, and low cost.^[26–29] With the introduction of Au NPs to Mn₃O₄, there is a significant activity enhancement.^[23,30] The reducible metal oxide can supply reactive oxygen species to Au's active sites.^[31] In particular, it has been suggested that the sites at the Au-support interface are responsible for the enhancement in the activity.^[32,33] To move ahead toward technological applications, it is of great interest to clarify the structure–performance relationship of Au-modified Mn₃O₄ catalysts.

Little is known about the effect of the surface structure of Mn₃O₄ on the redox interplay between Au and Mn₃O₄. To clarify the possible morphological effects of nanoscale Mn₃O₄ on the structure and activity of Au/Mn₃O₄ nanocomposites, in the present study, we synthesized three kinds of Mn₃O₄ NPs that were significantly different in morphology. They were then loaded with Au NPs and evaluated for the combustion of benzene. The Mn₃O₄ and Au/Mn₃O₄ samples were characterized by X-ray diffraction (XRD), N₂ sorption measurements, X-ray photoelectron spectroscopy (XPS), transmission electron microscopy (TEM), scanning electron microscopy (SEM), in situ infrared spectroscopy (in situ IR), hydrogen-temperature-programmed reduction (H₂-TPR), and oxygen-temperature-programmed desorption (O₂-TPD).

Results and Discussion

Figure 1 shows SEM images of the three kinds of Mn₃O₄ NPs: Figure 1a shows an image of cubes (ca. 65 nm in size) with smooth edges, which are denoted as Mn₃O₄ CPs; Figure 1b shows an image of morphologically uniform octahedrons (ca. 50 nm in size), which are denoted as Mn₃O₄ OPs; and Figure 1c shows images of hexagonal nanoplates with a

[a] Dr. Z.-Y. Fei, B. Sun, L. Zhao, Prof. W.-J. Ji
Key Laboratory of Mesoscopic Chemistry, MOE
School of Chemistry and Chemical Engineering, Nanjing University
Nanjing 210093 (P. R. China)
Fax: (+86)25-83317761
E-mail: jiwj@nju.edu.cn

[b] Prof. C.-T. Au
Department of Chemistry, Hong Kong Baptist University
Kowloon Tong (Hong Kong)
E-mail: pctau@hkbu.edu.hk

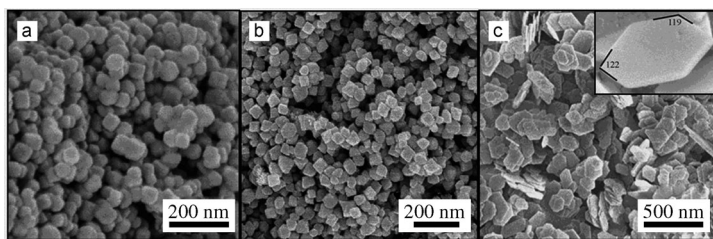


Figure 1. SEM images of a) Mn_3O_4 CPs, b) Mn_3O_4 OPs, and c) Mn_3O_4 HPs (the inset is the enlarged image of a Mn_3O_4 hexagonal nanoplate).

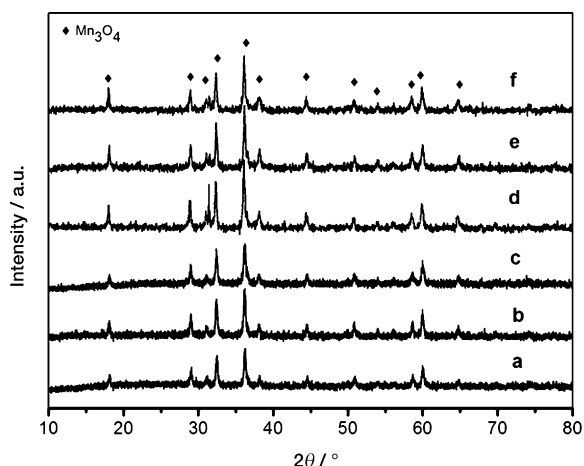


Figure 2. XRD patterns of a) Mn_3O_4 CPs, b) Mn_3O_4 HPs, c) Mn_3O_4 OPs, d) $\text{Au}/\text{Mn}_3\text{O}_4$ CPs, e) $\text{Au}/\text{Mn}_3\text{O}_4$ HPs, and f) $\text{Au}/\text{Mn}_3\text{O}_4$ OPs.

uniform morphology, which are denoted as Mn_3O_4 HPs. The average thickness and edge length of the nanoplates are approximately 20 and 200 nm, respectively.

The XRD patterns (Figure 2) of the three Mn_3O_4 samples reveal that they are identical in phase structure with the lattice constants $a=0.576$, $c=0.947$ nm, and $Z=4$ (JCPDS No. 24-0734). After the addition of the Au NPs, there is no change in the XRD patterns. The size, distribution, crystallinity and quantity of Au NPs could all affect the Au signal of the XRD pattern. Due to the calcination of $\text{Au}/\text{Mn}_3\text{O}_4$ (300°C), the crystallinity of the Au NPs is probably not be an important issue. The Au loading is only about 2 wt %, and moreover, the Au NPs are 3–4 nm in size and well distributed on the Mn_3O_4 substrates (see the TEM images below), which could account for the absence of a Au signal in the XRD patterns. Typical high-resolution TEM (HRTEM) images of the three kinds of Mn_3O_4 nanocrystallites with and without Au NP deposition are shown in Figure 3. The (101) planes, with a lattice space of 0.486 nm, and the set of (200) planes, with a crossing lattice space of 0.282 nm, can

be identified in the HRTEM images of Mn_3O_4 CPs. This observation suggests that Mn_3O_4 CPs are single crystals bound by the (101), (103), and (200) planes, in good agreement with the cube model (inset of Figure 3a). The Mn_3O_4 OPs show two sets of (101) planes with a lattice space of 0.486 nm, and the (200) planes are the only ones normal to the two sets of (101) planes. Another set of planes that make an angle of 62° with the (200) planes are the (103) planes, so the Mn_3O_4 OPs are single crystals bound by the (101), (103), and (200) planes, as illustrated by the octahedron model in the inset of Figure 3b. For Mn_3O_4 HPs, the dominant exposed planes are (200) and are normal to the set of (101) planes with a lattice space of 0.486 nm and the set of (103) planes with a square crossing lattice space of 0.273 nm. In Figure 3d–f, the Au particles can be readily observed and have a size in the range of 3–4 nm. The inductively coupled plasma-atomic emission spectroscopy (ICP-AES) analysis indicated the loading of Au was 1.9–2.0 wt % (Table 1). The Au NPs are statistically distributed over the oxygen-terminated (101), (103), and (200) surfaces of Mn_3O_4 CPs. Similarly, the Au NPs are statistically distributed over the oxygen-terminated (101), (103), and (200) surfaces of the Mn_3O_4 OPs. On the other hand, the Au NPs are pre-

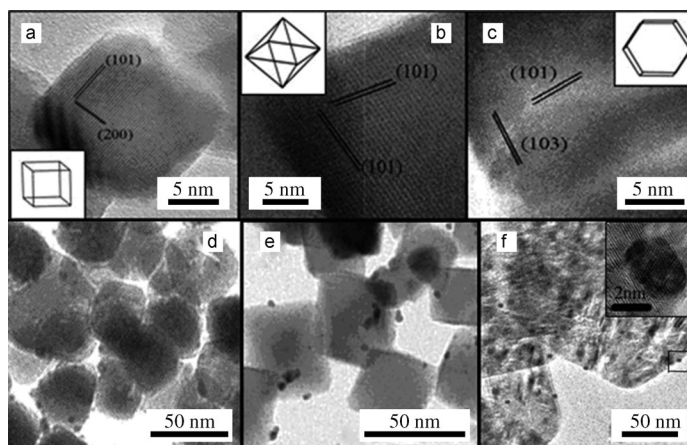


Figure 3. HRTEM images of a) Mn_3O_4 CPs, b) Mn_3O_4 OPs, c) Mn_3O_4 HPs, d) $\text{Au}/\text{Mn}_3\text{O}_4$ CPs, e) $\text{Au}/\text{Mn}_3\text{O}_4$ OPs, and f) $\text{Au}/\text{Mn}_3\text{O}_4$ HPs. The insets of a)–c) are the geometric models of the Mn_3O_4 nanocrystallites.

Table 1. Au loading, H_2 -TPR peak temperature, O_2 -TPD peak temperature, BET surface area, and catalytic activity.

Sample	Au loading ^[a] [wt. %]	d_{Au} ^[b] [nm]	S_{BET} [$\text{m}^2 \text{g}^{-1}$]	H_2 -TPR peaks [$^\circ\text{C}$]	O_2 -TPD peaks [$^\circ\text{C}$]	T_{10}/T_{90} ^[c] [$^\circ\text{C}$]	r_{A} ^[d] [$\mu\text{mol} \text{m}^{-2} \text{h}^{-1}$]
Mn_3O_4 CPs	without Au	NA	22.6	473	174/449	195/289	5.8
Mn_3O_4 OPs	without Au	NA	26.1	485	173/421	212/297	4.5
Mn_3O_4 HPs	without Au	NA	20.5	443	165/422	183/262	7.2
$\text{Au}/\text{Mn}_3\text{O}_4$ CPs	1.93	3	20.6	243/450	144/409	156/231	5.2
$\text{Au}/\text{Mn}_3\text{O}_4$ OPs	1.95	3	21.1	353/477	148/406	165/246	4.1
$\text{Au}/\text{Mn}_3\text{O}_4$ HPs	1.97	4	20.1	199/402	138/408	151/212	8.1

[a] Determined by ICP-AES analysis. [b] Average particle size of Au NPs based on TEM results; NA: Not available. [c] Temperatures at which conversion of benzene were 10 (T_{10}) and 90% (T_{90}). [d] Specific activities of benzene oxidation at 200°C for $\text{Au}/\text{Mn}_3\text{O}_4$ and 250°C for Mn_3O_4 .

dominantly distributed on the topmost oxygen layers of the (200) orientation of the Mn_3O_4 HPs.

The BET surface areas of the samples are shown in Table 1. The order of specific surface areas is Mn_3O_4 OPs (26.1) > Mn_3O_4 CPs (22.6) > Mn_3O_4 HPs ($20.5 \text{ m}^2 \text{ g}^{-1}$). The observed trend can be explained by the size of the corresponding Mn_3O_4 crystallites. After the deposition of Au particles, BET surface areas of 20.1, 20.6, and $21.1 \text{ m}^2 \text{ g}^{-1}$ are obtained for Au/ Mn_3O_4 HPs, Au/ Mn_3O_4 CPs, and Au/ Mn_3O_4 OPs, respectively. The BET surface areas of Au/ Mn_3O_4 samples are found to decrease to certain degree after the deposition of Au NPs on the Mn_3O_4 nanocrystallites. Since the density of Au is much higher than that of Mn_3O_4 , the contribution of Au NPs to the overall surface area is negligible, in other words, the incorporation of Au NPs may cause a decrease in surface area of about 2%. On the other hand, a portion of the smallest Mn_3O_4 nanocrystallites with incorporated Au NPs could flow away during the Au loading step. Such a phenomenon would be more notable for the Au loading on Mn_3O_4 OPs, since the size of the Mn_3O_4 OPs is smaller than that of the CPs or HPs (Figure 1), leading to a more apparent decrease in the BET surface area. The BET surface areas could affect the catalytic activity, while the specific activity data shown in Table 1 (normalized per unit surface area) are not influenced by the overall surface area. The activity order of Au/ Mn_3O_4 HPs > Au/ Mn_3O_4 CPs > Au/ Mn_3O_4 OPs is clearly observable in Table 1.

Based on the geometric models proposed from the TEM/SEM observations, the average percent area of each facet can be estimated (Table 2). By correlating the overall activi-

Table 2. Area percentage of (101), (200), and (103) planes for the three kinds of Mn_3O_4 polyhedrons, estimated based on TEM/SEM results (averaged).

Sample	(101) [%]	(200) [%]	(103) [%]
Mn_3O_4 CPs	33.3	33.3	33.3
Mn_3O_4 OPs	50	25	25
Mn_3O_4 HPs	0	93	7

ty of three Au/ Mn_3O_4 systems with the percent area of (101), (200), and (103) planes for the corresponding Mn_3O_4 polyhedrons (Table 2), one can deduce the activity order of the Au-support interfaces: Au/(200) \approx Au/(103) > Au/(101).

The redox behaviors of Mn_3O_4 and Au/ Mn_3O_4 , as studied by H_2 -TPR and O_2 -TPD, are shown in Figures 4 and 5 and Table 1. The H_2 -TPR profiles of Mn_3O_4 nanocrystallites show broad peaks in the 440–490 °C range: Mn_3O_4 OPs at 485 °C, Mn_3O_4 CPs at 473 °C, and Mn_3O_4 HPs at 443 °C. These results imply that the lattice oxygen of Mn_3O_4 HPs should have the highest reactivity.^[34] The deposition of Au NPs onto the Mn_3O_4 substrates results in additional reduction peaks in the 100–400 °C range, and the reducibility follows the following order: Au/ Mn_3O_4 HPs > Au/ Mn_3O_4 CPs > Au/ Mn_3O_4 OPs. A comparison of the H_2 -TPR profiles of the Au-loaded samples with those of their Mn_3O_4 counterparts reveals that the presence of Au NPs slightly promotes the

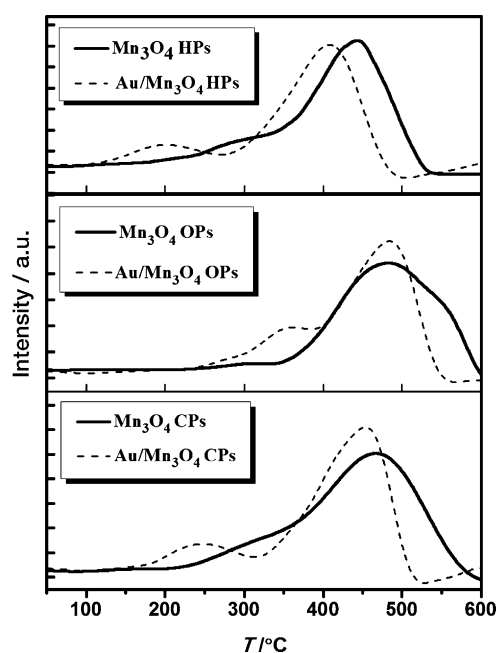


Figure 4. H_2 -TPR profiles of the Mn_3O_4 nanocrystallites with and without Au deposition.

reduction of Mn_3O_4 , as reflected by a 10–40 °C decrease in the main reduction peaks.

Figure 5 shows the O_2 -TPD profiles of the samples. The desorption peak below 300 °C can be ascribed to the desorption of oxygen adspecies, such as O_2^- and O^- , while the de-

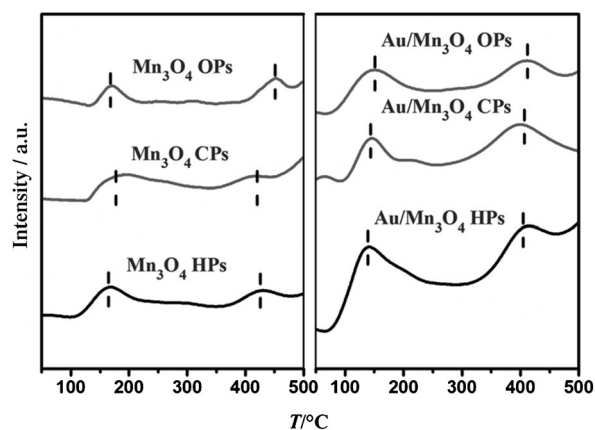


Figure 5. O_2 -TPD profiles of the three kinds of Mn_3O_4 nanocrystallites with and without Au deposition.

sorption peak above 500 °C can be attributed to the desorption of lattice oxygen.^[35] Generally, the desorption peaks in the 100–300 °C range correspond to oxygen adspecies that are active for catalytic oxidation.^[36]

The amount of weakly adsorbed oxygen species (such as O_2^- and O^-) on Mn_3O_4 HPs is larger than that on Mn_3O_4 CPs or Mn_3O_4 OPs. Note that, after Au loading, the amount of weakly adsorbed oxygen species increases significantly,

especially in the case of Au/Mn₃O₄ HPs. The desorption peak of weakly adsorbed oxygen species shifts to 140 °C on Au/Mn₃O₄ HPs, while it shifts to 150 and 160 °C on Au/Mn₃O₄ CPs and Au/Mn₃O₄ OPs, respectively, indicating that among the three Au-loaded samples, Au/Mn₃O₄ HPs shows the weakest adsorption bond for weakly adsorbed oxygen species.

The XPS Au 4f, O 1s and Mn 2p spectra of the Au/Mn₃O₄ composites are presented in Figure 6. There are broad Au 4f_{7/2} and 4f_{5/2} peaks observed across the Au/Mn₃O₄ sam-

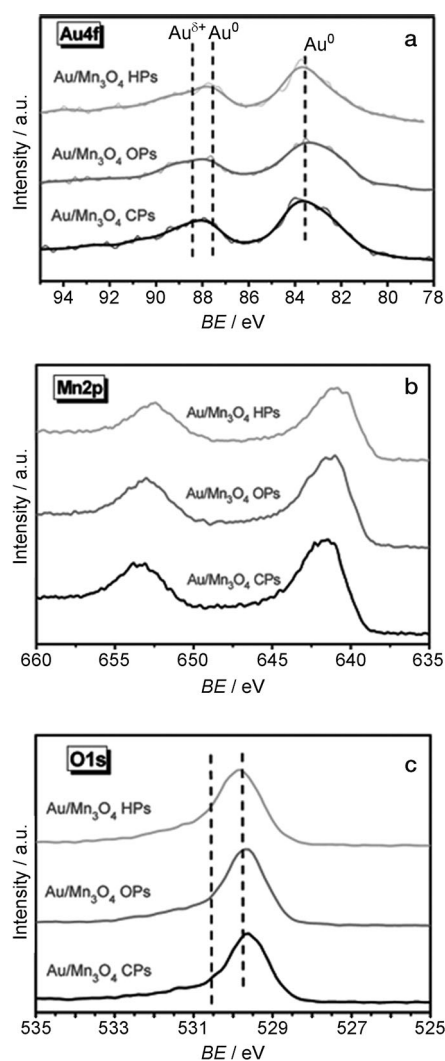


Figure 6. XPS Au 4f, Mn 2p, and O 1s spectra of Au/Mn₃O₄ samples.

ples (Figure 6a). There are naturally two kinds of Mn cations in Mn₃O₄, namely, Mn²⁺ and Mn³⁺, accounting for the multiple Mn states detected by XPS. The binding energies of Au 4f_{7/2} (83.7 eV) and Au 4f_{5/2} (87.5 eV) suggest that the Au NPs exist mostly in a metallic form. The signals at approximately 88.6 eV, however, indicate that a fraction of Au atoms (plausibly those of the topmost layer) could be in a partially oxidized state (δ^+). The more intense shoulders at

88.6 eV show that the Au clusters in Au/Mn₃O₄ CPs and Au/Mn₃O₄ OPs are more electron deficient. The surface composition and chemical state of the Mn₃O₄ substrates (Figure 6b) are similar for the three samples with Au loading. Figure 6c shows the O 1s spectra of Au/Mn₃O₄ samples. The O 1s peak at 529.8 eV may be assigned to lattice oxygen species (O²⁻) and the one at 530.3 eV to oxygen species (such as O⁻ species) with an electron density lower than that of O²⁻ ions. The number of oxygen vacancies can be related to the variation of the area ratio of oxygen adspecies (O⁻) to lattice oxygen (O²⁻), which follows the order of Au/Mn₃O₄ HPs > Au/Mn₃O₄ OPs > Au/Mn₃O₄ CPs, suggesting that there is a higher density of O⁻ species on Au/Mn₃O₄ HPs, consistent with the O₂-TPD results.

The diffuse reflectance infrared Fourier transform (DRIFT) spectra of the Mn₃O₄ and Au/Mn₃O₄ samples recorded during benzene oxidation are presented in Figure 7.

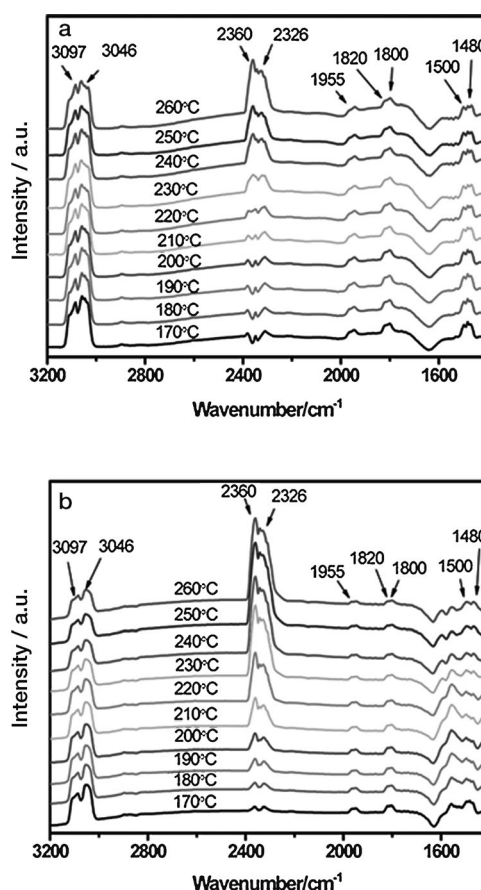


Figure 7. DRIFT spectra of benzene oxidation over a) Mn₃O₄ CPs, and b) Au/Mn₃O₄ CPs at temperatures within the 170–260 °C range.

There are a number of bands in the 1400–3500 cm⁻¹ region. The bands at 2360 and 2326 cm⁻¹ can be ascribed to the asymmetric stretching mode ($\nu_{as}(\text{OCO})$) of molecularly adsorbed CO₂.^[37] The bands at 3097 and 3046 cm⁻¹ are attributed to the stretching vibration of aromatic =C–H groups, and the bands at 1800 and 1955 cm⁻¹ are attributable to the

C–H out-of-plane vibrations of adsorbed benzene.^[38] The bands at 1500 and 1480 cm⁻¹ are attributed to the stretching vibration of aromatic nuclei (C=C, Π_g⁶) of benzene in the gas phase and adsorbed state, respectively.^[39] Based on the evolution of the bands arising from CO₂ (product) as well as the elimination of the bands from benzene (reactant) in the course of the reaction, one can infer that the Au/Mn₃O₄ composites are clearly more active than the Mn₃O₄ substrates. The observation is further confirmed by the results of a continuous-flow reaction in a fixed-bed reactor (see below). Apart from C₆H₆ and CO₂, no other species are detected than the Mn₃O₄ nanocrystallites and the Au/Mn₃O₄ composites during DRIFT measurements, indicating the complete oxidation of benzene to CO₂.

Previous studies on manganese oxide based catalysts for VOC combustion showed that features such as bulk oxygen mobility, the reducibility of manganese oxide, and the method of metal deposition on manganese oxide have critical effects on VOC oxidation.^[28,40–42] A catalyst with a higher reducibility and substrate-lattice oxygen mobility performs better in the oxidation reactions^[43,44] and under these circumstances, the reaction on the substrate may follow a Mars–Van Krevelen (MVK) mechanism.^[45] The oxidation that occurs on supported noble metals is believed to follow the Langmuir–Hinshelwood (L–H) mechanism in which the rate-determining step is the surface reaction between two adjacent adsorbed molecules.^[46] On the other hand, hydrocarbons undergo oxidation through a superficial reaction mechanism at temperatures <400 °C that involves oxygen adspecies on the surface oxygen vacancies of the catalyst.^[47,48] The O₂-TPD results collected from the present samples suggest that, with Au deposition on the Mn₃O₄ substrates of different morphologies, there is an enhanced concentration and reactivity of oxygen adspecies. In line with such an enhancement, there is enhanced catalytic activity in benzene combustion (Figure 8). The T₁₀ and T₉₀ temperatures, at which 10 and 90% benzene conversions are achieved, respectively, are given in Table 1. Clearly, the mor-

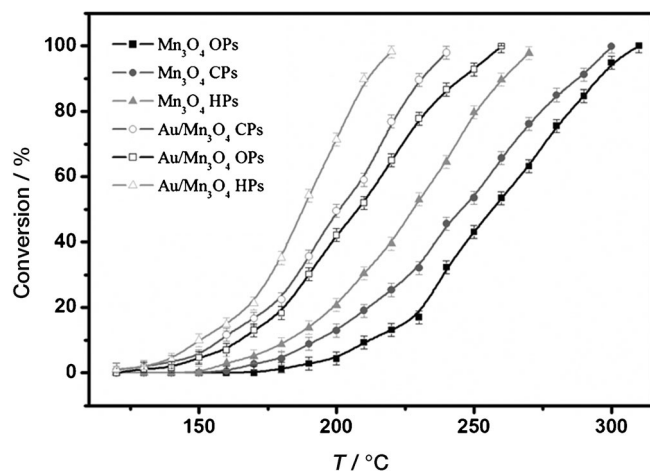


Figure 8. Catalytic activities for benzene combustion as a function of reaction temperature for the Mn₃O₄ NPs and the Au-loaded samples.

phology of the Mn₃O₄ substrates shows an effect on benzene combustion: Mn₃O₄ HPs outperforms Mn₃O₄ CPs and Mn₃O₄ OPs, while Au/Mn₃O₄ HPs are more active than Au/Mn₃O₄ OPs and Au/Mn₃O₄ CPs. Based on the specific rates of benzene conversion (per unit surface area of catalyst) at 250 °C, values of 7.2, 5.8, and 4.5 μmol m⁻² h⁻¹ are derived for Mn₃O₄ HPs, Mn₃O₄ CPs, and Mn₃O₄ OPs, respectively. For the Au-loaded samples, the average specific activities at 200 °C are 8.1, 5.2, and 4.2 μmol m⁻² h⁻¹, for Au/Mn₃O₄ HPs, Au/Mn₃O₄ CPs, and Au/Mn₃O₄ OPs, respectively. Note that the catalytic activity trends are similar over the Mn₃O₄ substrates and the Au-loaded samples. Considering the comparable distribution of Au NPs on the three Mn₃O₄ substrates, one can reasonably infer that the morphological impact of each Mn₃O₄ substrate on the reaction is retained for the corresponding Au/Mn₃O₄ composite. In other words, the enhanced activity of Au/Mn₃O₄ HPs, Au/Mn₃O₄ OPs, and Au/Mn₃O₄ CPs should be attributed to the effect of the Au–Mn₃O₄ boundary, at which the electronic modification of the Au NPs and the structure of the Mn₃O₄ substrate have a joint effect.

Based on the areal percent distribution of each facet shown in Table 2, one can estimate the specific activity of (101), (200), and (103) planes of the Mn₃O₄ substrates; the results are shown in Table 3. The (103) and (200) planes are

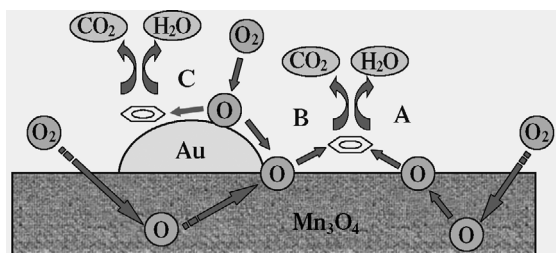
Table 3. Specific activity of (101), (200), and (103) planes.^[a]

Sample	(101) [μmol m ⁻² h ⁻¹]	(200) [μmol m ⁻² h ⁻¹]	(103) [μmol m ⁻² h ⁻¹]
Mn ₃ O ₄ nanocrystallites ^[b]	0.6	7.0	7.5

[a] Calculated based on the average surface area percentages of each facet and specific activity of each catalyst. [b] Specific activity at 250 °C for Mn₃O₄.

much more active than the (101) planes for benzene combustion. The observed geometric effect of Mn₃O₄ facets on the catalytic activity is presumably related to the nature and density of Mn⁴⁺ and oxygen vacancies, which are responsible for the adsorption/activation of benzene or oxygen molecules. The O₂-TPD results (Figure 5) in part support this inference. One should bear in mind that the overall activity is determined by a complicated synergism between the specific crystal surface, the atomic arrangement, and the particle size.

It is known that surface oxygen species exert a notable influence on the catalytic activity in oxidation reactions.^[47] As shown in Scheme 1, benzene can be oxidized over Au/Mn₃O₄ through three possible pathways. In path A, benzene on Mn₃O₄ is oxidized by oxygen originating from Mn₃O₄, following the MVK mechanism, as well as weakly adsorbed oxygen species. Existing research suggests that the MVK mechanism is a reasonable explanation of the total oxidation of VOCs over metal oxides such as Mn₃O₄,^[28] Co₃O₄^[43] and others.^[49] In our case, the MVK mechanism contributes to the overall benzene combustion activity. As Au is loaded on these facets, there is a synergetic effect arising from in-



Scheme 1. Possible reaction pathways of benzene oxidation over Mn₃O₄ nanocrystallites and their Au-modified counterparts, Au/Mn₃O₄.

tense interactions between the electronically rich Au nanoclusters and the Mn₃O₄ surfaces, which weakens the Mn–O bond at the Au–Mn₃O₄ boundary. This deduction is supported by the H₂-TPR results. In reaction path B, benzene is oxidized by lattice oxygen close to the Au–Mn₃O₄ boundary. Here, there is another possibility, that is, the oxygen adspecies on the Au NPs can migrate to the Au–Mn₃O₄ boundary (spillover effect) and react with the adsorbed benzene molecules nearby. This reaction path can be regarded as a modification of path B, since there is a dynamic transformation between surface-adsorbed and surface-lattice oxygen species. Changing the ratio of Au to Mn can certainly influence the activity and selectivity (either positively or negatively). Ideally, if interfaces of the same kind can be increased by increasing the ratio of Au to Mn in parallel, then the outcome shall be beneficial for the reaction. Unfortunately, it is technically challenging to enhance the interfaces while maintaining their original nature by simply increasing the ratio of Au to Mn. This is because increasing the Au loading inevitably causes a change in the Au particle size, which in turn leads to a change in the surface state and electronic properties of Au NPs^[50] and, consequently, the nature of the Au–Mn₃O₄ interfaces. In the present study, relatively low Au loading (1.9–2.0%) was used for the three Mn₃O₄ nanocrystallites of different morphologies to generate Au particles of 3–4 nm and to achieve comparable Au dispersion over the three Mn₃O₄ substrates.

In path C, benzene can be attacked by adjacent oxygen adspecies on the Au NPs. In situ FTIR studies, we do not detect any additional benzene adsorption states over the Au/Mn₃O₄ catalysts, suggesting that path C is insignificant for benzene combustion. To summarize, path A is important for benzene combustion on the Au-free Mn₃O₄ substrates, while reaction paths A, B, and a modified version of B (especially the last two) are critical for benzene combustion on the Au-deposited Mn₃O₄ composites.

Figure 9 shows a stability test for Au/Mn₃O₄ HPs at T_{100} . The catalyst exhibits good stability over a period of 30 h. Reaction cycling between T_{50} and T_{90} was also conducted, and the results indicate that there was no deactivation during the cycles between T_{50} and T_{90} .

The activation energies (E_a) were estimated over the Mn₃O₄ substrates and their Au-deposited counterparts (Figure 10). The E_a values for Au/Mn₃O₄ OPs, Au/Mn₃O₄

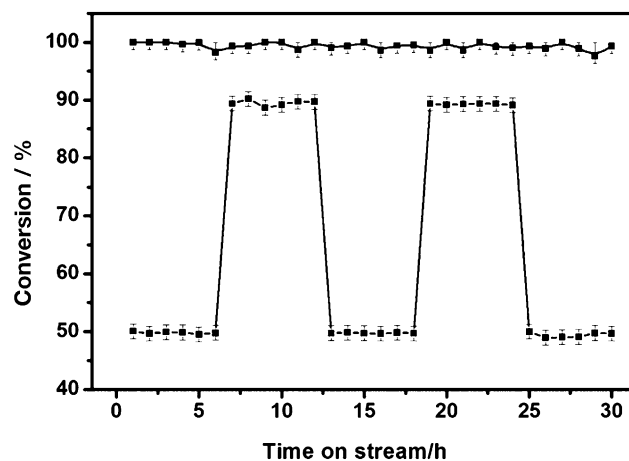


Figure 9. Stability tests of Au/Mn₃O₄ HPs at T_{100} and cycle reactions between T_{50} and T_{90} .

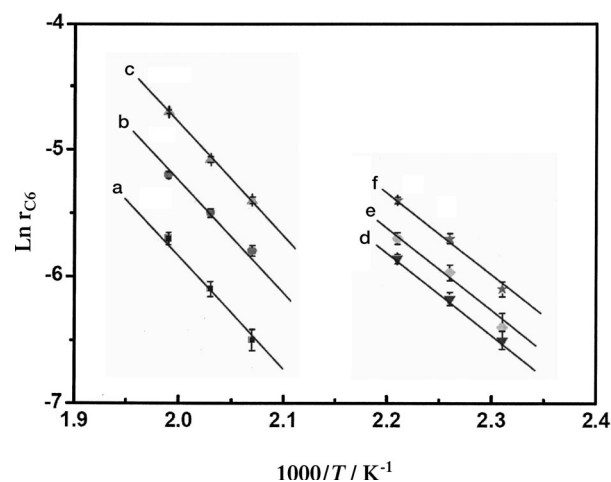


Figure 10. Arrhenius plots: (a) Mn₃O₄ OPs, (b) Mn₃O₄ CPs, (c) Mn₃O₄ HPs, (d) Au/Mn₃O₄ OPs, (e) Au/Mn₃O₄ CPs, and (f) Au/Mn₃O₄ HPs.

CPs, and Au/Mn₃O₄ HPs (54.4, 53.1, and 52.6 kJ mol⁻¹, respectively) are lower than those for Mn₃O₄ OPs, Mn₃O₄ CPs, and Mn₃O₄ HPs (62.5, 62.3, and 58.0 kJ mol⁻¹, respectively) and confirm the enhanced reactivity of the Au–Mn₃O₄ catalysts.

Oxygen labeling is helpful to understand reaction mechanisms involving oxygen species, especially the origin of the oxygen in the products. In the present Au/Mn₃O₄ system, however, a complication could occur: even though the spillover of oxygen adspecies from Au NPs onto the Mn₃O₄ substrate is fast enough, the oxygen isotope exchange over the Mn₃O₄ substrate may be more rapid than the rate of benzene oxidation. Additionally, there is a possibility for exchange between the reaction products and ¹⁸O₂. These circumstances make this technique technically invalid for distinguishing the parallel reaction pathways. Nevertheless, a follow up study on the oxygen isotope exchange, together with the reaction of benzene and ¹⁸O₂, on the individual Mn₃O₄ substrates and the corresponding Au/Mn₃O₄ compo-

sites, may be helpful to further understand the reaction mechanism.

Conclusion

The present study demonstrates that the catalytic activities of (101), (200), and (103) facets of Mn_3O_4 nanocrystallinities in benzene combustion are clearly different. When Au is loaded on these surfaces, the activities are notably enhanced due to the synergetic effects arising from intense metal–support interactions between the electronically modified Au nanoclusters and the substrate surfaces, resulting in the weakening of Mn–O bonds at the Au– Mn_3O_4 boundary. Reaction path A (Scheme 1), in which benzene on Mn_3O_4 is oxidized by the released oxygen from Mn_3O_4 through a MVK mechanism as well as by the weakly adsorbed oxygen species, is important for Au-free Mn_3O_4 substrates, while reaction path B, in which benzene is oxidized by the lattice oxygen around the Au– Mn_3O_4 boundary, becomes more critical for the Au-deposited Mn_3O_4 . The oxygen species activated on the Au NPs can spillover onto the Au– Mn_3O_4 boundary and react with the neighboring benzene molecules. This can be regarded as a modified version of path B. H_2 -TPR, O_2 -TPD and in situ FTIR characterizations were used to elucidate the main reaction pathways described above and further clarified the early presumption that the metal–substrate boundary is the key region for the reaction.

Experimental Section

Catalyst preparation

Synthesis of Mn_3O_4 CPs: In a typical procedure, $\text{Mn}(\text{CH}_3\text{COO})_2 \cdot 4\text{H}_2\text{O}$ (1.25 g) was dissolved in distilled water (100 mL). Then, ammonium hydroxide (2 mL) and distilled water (58 mL) were mixed and added to the manganese acetate solution under continuous stirring. After that, NaOH (1 M, 10 mL) was added dropwise to the above solution under stirring for 30 min. Then, the mixture was transferred into a 200 mL Teflon-lined stainless steel autoclave and heated at 160 °C for 12 h. The brown precipitate was collected by centrifugation, washed several times with distilled water and absolute ethanol, dried at 80 °C under vacuum for 3 h, calcined at 300 °C under air atmosphere for 3 h, and cooled to RT under nitrogen.

Synthesis of Mn_3O_4 HPs: The procedure is similar to that of the synthesis of Mn_3O_4 CPs, except without the addition of ammonium hydroxide and with more NaOH solution (1 M, 70 mL).

Synthesis of Mn_3O_4 OPs: The procedure is similar to that of the synthesis of Mn_3O_4 HPs, except that a NaOH solution (1 M, 70 mL) was replaced by an ammonium hydroxide solution (1 M, 70 mL).

Preparation of Au/ Mn_3O_4 samples

Gold NPs were deposited on the as-synthesized manganese oxides of different morphologies with a nominal Au loading of 2 wt % by means of deposition–precipitation (DP), originally adopted by Haruta et al.^[18] In a typical procedure, the Mn_3O_4 substrates were dispersed in an aqueous solution of HAuCl_4 at a fixed pH of 10. The suspension was aged at 333 K for 2 h. The solid was filtered out, washed several times with distilled water, and dried at 373 K in air for 10 h. Then the samples were calcined at 573 K for 4 h in flowing N_2 . The Au-containing catalysts are denoted herein as Au/ Mn_3O_4 HPs, Au/ Mn_3O_4 CPs, and Au/ Mn_3O_4 OPs.

Characterization of catalysts

Powder X-ray diffraction (XRD) was performed (2θ : 10 to 80°) on a Philips X'Pert Pro diffractometer with $\text{Cu}_{\text{K}\alpha}$ radiation (0.1541 nm). The size and morphology of the as-synthesized samples were determined with a JEOL JEM-1010 TEM at an accelerating voltage of 80 kV. HRTEM images were taken using a JEOL JEM-2100 electron microscope operated at 200 kV.

The BET surface area was measured on a NOVA-1200 material physical structure determinator based on the N_2 adsorption and desorption isotherms at 77 K. Prior to measurements, all samples were degassed at 573 K for 4 h. Elemental analysis of Au was performed using ICP-AES on a J-A1100 Versa Probe spectrometer. The samples were dissolved in a mixture of concentrated HCl and HNO_3 with a volumetric ratio of 3:1 prior to analysis.

H_2 -TPR measurements using a H_2 -Ar mixture (4.98% H_2 by volume) were carried out with the sample installed in a U-shaped quartz reactor connected to a thermal conduction detector (TCD); a set amount of sample (50 mg) was used for each measurement. Before switching to the H_2 -Ar stream, the sample was treated in an Ar stream at 120 °C for 1 h and then cooled to RT. Temperature programming was performed in the 50–500 °C range at a rate of 10 °C min^{-1} . Temperature-programmed desorption (TPD) of O_2 was also carried out using the U-shaped quartz reactor. The catalyst (200 mg) was pretreated in an Ar stream at 500 °C for 1 h, and oxygen adsorption proceeded with exposure to pure O_2 at 200 °C for 0.5 h. After cooling to room temperature, the sample was purged with Ar (60 mL min^{-1}) for 1 h. The sample was then heated to 800 °C at a rate of 10 °C min^{-1} in the Ar flow (60 mL min^{-1}), and the effluent gases were analyzed by a TCD.

In situ IR spectra were recorded (in the 1400–3500 cm^{-1} region, resolution: 4 cm^{-1}) on a Bruker VERTEX70 spectrometer using the DRIFT technique. Before IR measurements, the sample was swept with air at 200 °C for 1 h. Then, a gas mixture of 1000 ppm benzene plus balanced dry air was continuously passed through the sample cell. The spectra were collected at the designated temperatures.

Catalyst activity tests and kinetic measurements

The catalysts were evaluated at atmospheric pressure using a fixed-bed quartz reactor. The sample (400 mg) was diluted with chemically inert SiC. Before reaction, the sample was kept in a flow of air (40 mL min^{-1}) at 200 °C for 1 h. Benzene vapor was carried by an air stream bubbling in a benzene saturator stationed in an ice bath. The benzene-saturated air was further diluted by another air stream before reaching the catalyst bed. The concentration of benzene in the feed was controlled by adjusting the flow rate of the air stream passing through the saturator. The total flow rate was approximately 40 mL min^{-1} . The temperature was raised stepwise with an interval of 10 °C from 150 °C to a temperature at which complete conversion of benzene was achieved. The data presented at each temperature are the averaged values of three measurements. The unreacted benzene and products were analyzed online using a gas chromatograph equipped with a HP FFAP column (0.32 mm \times 25 m) and a flame-ionization detector. The permanent gas products were analyzed online by another gas chromatograph equipped with a packed column of Alltech Hayesep D HP and a TCD. The differences between the inlet and outlet concentrations of benzene were used to calculate conversion data. No carbon-containing product other than CO_2 was detected (carbon balance based on benzene and CO_2 with $\pm 3\%$ accuracy). Without the use of a catalyst, the reactivity was negligible under the conditions adopted in the present work.

Acknowledgements

Financial support from the Ministry of Science and Technology of China (2013AA031703) is greatly appreciated.

[1] S. Iijima, *Nature* **1991**, 354, 56–58.

[2] R. A. Pai, R. Humayun, M. T. Schulberg, A. Sengupta, J. N. Sun, J. J. Watkins, *Science* **2004**, 303, 507–510.

- [3] H. G. Yang, C. H. Sun, S. Z. Qiao, J. Zou, G. Liu, S. C. Smith, H. M. Cheng, G. Q. Lu, *Nature* **2008**, *453*, 638–641.
- [4] H. G. Yang, G. Liu, S. Z. Qiao, C. H. Sun, Y. G. Jin, S. C. Smith, J. Zou, H. M. Cheng, G. Q. Lu, *J. Am. Chem. Soc.* **2009**, *131*, 4078–4083.
- [5] R. Si, M. Flytzani-Stephanopoulos, *Angew. Chem.* **2008**, *120*, 2926–2929; *Angew. Chem. Int. Ed.* **2008**, *47*, 2884–2887.
- [6] L. Hu, Q. Peng, Y. Li, *J. Am. Chem. Soc.* **2008**, *130*, 16136–16137.
- [7] X. Xie, Y. Li, Z.-Q. Liu, M. Haruta, W. J. Shen, *Nature* **2009**, *458*, 746–749.
- [8] K. Zhou, X. Wang, X. Sun, Q. Peng, Y. D. Li, *J. Catal.* **2005**, *229*, 206–212.
- [9] A. Gluhoi, N. Bogdanchikova, B. Nieuwenhuys, *Catal. Today* **2006**, *113*, 178–181.
- [10] C. H. Ma, Z. Mu, J. Li, Y. Jin, J. Cheng, G. Lu, Z. Hao, S. Qiao, *J. Am. Chem. Soc.* **2010**, *132*, 2608–2613.
- [11] R. Zanella, S. Giorgio, C. Shin, C. Henry, C. Louis, *J. Catal.* **2004**, *222*, 357–367.
- [12] V. Schwartz, D. Mullins, W. Yan, B. Chen, S. Dai, S. Overbury, *J. Phys. Chem. B* **2004**, *108*, 15782–15790.
- [13] Y. Han, Z. Zhong, K. Ramesh, F. Chen, L. Chen, *J. Phys. Chem. C* **2007**, *111*, 3163–3170.
- [14] K. Qian, W. Huang, Z. Jiang, H. Sun, *J. Catal.* **2007**, *248*, 137–141.
- [15] G. Bond, D. Thompson, *Catal. Rev. Sci. Eng.* **1999**, *41*, 319–388.
- [16] A. S. K. Hashmi, G. J. Hutchings, *Angew. Chem.* **2006**, *118*, 8064–8105; *Angew. Chem. Int. Ed.* **2006**, *45*, 7896–7936.
- [17] B. K. Min, C. M. Friend, *Chem. Rev.* **2007**, *107*, 2709–2724.
- [18] M. Haruta, S. Tsubota, T. Kobayashi, H. Kageyama, M. J. Genet, B. Delmon, *J. Catal.* **1993**, *144*, 175–192.
- [19] N. M. Gupta, A. K. Tripathi, *Gold Bull.* **2001**, *34*, 120–128.
- [20] S. Carrettin, P. Concepción, A. Corma, J. M. Lopez Nieto, V. F. Puntes, *Angew. Chem.* **2004**, *116*, 2592–2594; *Angew. Chem. Int. Ed.* **2004**, *43*, 2538–2540.
- [21] L. Guzzi, A. Beck, K. Frey, *Gold Bull.* **2009**, *42*, 5–12.
- [22] X. Huang, H. Sun, L. Wang, Y. Liu, K. Fan, Y. Cao, *Appl. Catal. B* **2009**, *90*, 224–232.
- [23] R. M. Torres Sanchez, A. Ueda, K. Tanaka, M. Haruta, *J. Catal.* **1997**, *168*, 125–127.
- [24] S. D. Gardner, G. B. Hoflund, M. R. Davidson, D. R. Schryer, J. Schryer, B. T. Upchurch, E. J. Kielin, *Langmuir* **1991**, *7*, 2135–2140.
- [25] R. Zanella, S. Giorgio, C. R. Henry, C. Louis, *J. Phys. Chem. B* **2002**, *106*, 7634–7642.
- [26] G. G. Xia, Y. G. Yin, W. S. Willis, J. Y. Wang, S. L. Suib, *J. Catal.* **1999**, *185*, 91–105.
- [27] K. Ramesh, L. Chen, F. Chen, Z. Zhong, J. Chin, H. Mook, Y. F. Han, *Catal. Commun.* **2007**, *8*, 1421–1426.
- [28] V. P. Santos, M. F. R. Pereira, J. J. M. Orfao, J. L. Figueiredo, *Appl. Catal. B* **2010**, *99*, 353–363.
- [29] Y. F. Han, L. Chen, K. Ramesh, E. Widjaja, S. Chilukoti, I. K. Surjami, J. Chen, *J. Catal.* **2008**, *253*, 261–268.
- [30] L. Wang, Q. Liu, X. Huang, Y. Liu, Y. Cao, K. Fan, *Appl. Catal. B* **2009**, *88*, 204–212.
- [31] M. M. Schubert, S. Hackenberg, A. C. V. Veen, M. Muhler, V. Plzak, R. J. Behm, *J. Catal.* **2001**, *197*, 113–122.
- [32] M. Haruta, *Catal. Today* **1997**, *36*, 153–166.
- [33] M. M. Schubert, M. J. Kahlich, H. A. Gasteiger, R. J. Behm, *J. Power Sources* **1999**, *84*, 175–182.
- [34] P. Li, C. He, J. Cheng, C. Y. Ma, B. J. Dou, Z. P. Hao, *Appl. Catal. B* **2011**, *101*, 570–579.
- [35] L. Xue, C. Zhang, H. He, Y. Teraoka, *Appl. Catal. B* **2007**, *75*, 167–174.
- [36] Z. P. Hao, D. Y. Cheng, Y. Guo, Y. H. Liang, *Appl. Catal. B* **2001**, *33*, 217–222.
- [37] A. Berná, A. Kuzume, E. Herrero, J. M. Feliu, *Surf. Sci.* **2008**, *602*, 84–94.
- [38] S. Todorova, B. L. Su, *J. Mol. Catal. A: Chem.* **2003**, *201*, 223–235.
- [39] J. Q. Fu, C. H. Ding, *Catal. Commun.* **2005**, *6*, 770–776.
- [40] S. C. Kima, W. G. Shimb, *Appl. Catal. B* **2010**, *98*, 180–185.
- [41] M. Ousmane, L. F. Liotta, G. D. Carloe, G. Pantaleod, A. M. Venezia, *Appl. Catal. B* **2011**, *101*, 629–637.
- [42] B. Solsonaa, T. Garciab, S. Agouram, G. J. Hutchings, S. H. Taylor, *Appl. Catal. B* **2011**, *101*, 388–396.
- [43] B. Solsona, T. E. Davies, T. Garcia, I. Vázquez, A. Dejoz, S. H. Taylor, *Appl. Catal. B* **2008**, *84*, 176–184.
- [44] I. Rossetti, L. Forni, *Appl. Catal. B* **2001**, *33*, 345–352.
- [45] K. S. Song, D. Klvana, J. Kirchnerova, *Appl. Catal. A* **2001**, *213*, 113–121.
- [46] H. Shinjoh, H. Muraki, Y. Fujitani, *Appl. Catal.* **1989**, *49*, 195–204.
- [47] R. J. H. Voorhoeve, J. P. Remeika, D. W. Johnson, *Science* **1973**, *180*, 62–64.
- [48] Y. Z. Wang, Y. X. Zhao, C. G. Gao, D. S. Liu, *Catal. Lett.* **2008**, *125*, 134–138.
- [49] B. K. Hodnett, in *Heterogeneous Catalytic Oxidation*, Wiley, Chichester, **2000**, pp. 86–90.
- [50] D. C. Meier, X. F. Lai, D. W. Goodman, in *Surface Chemistry and Catalysis*, (Eds.: A. F. Carley, P. R. Davies, G. J. Hutchings, M. S. Spencer), Kluwer/Plenum, New York, **2002**, pp. 147–189.

Received: November 17, 2012
Published online: March 22, 2013